Diffuse x-ray scattering from stacking faults in *a*-plane GaN epitaxial layers

M. Barchuk and V. Holý
Department of Condensed Matter Physics, Faculty of Mathematics and Physics, Charles University, Ke Karlovu 5, CZ-121 16 Prague 2, Czech Republic

D. Kriegner and J. Stangl
Institute of Semiconductor and Solid State Physics, Johannes Kepler University Linz, Altenbergerstr. 69, AT-4040 Linz, Austria

S. Schwaiger and F. Scholz
Institute of Optoelectronics, University of Ulm, DE-89069 Ulm, Germany

(Received 25 July 2011; published 23 September 2011)

Diffuse x-ray scattering from various types of stacking faults in basal (0001) planes in *a*-oriented wurtzite GaN epitaxial layers is described theoretically and the calculated intensity distributions are compared with experimental data. From the comparison, the densities of stacking faults in a series of *a*-GaN samples were determined. The method makes it possible to discriminate the diffuse scattering from stacking faults from the influence of nonplanar defects like dislocations.

DOI: 10.1103/PhysRevB.84.094113 PACS number(s): 61.05.cp, 61.72.Nn, 81.05.Ea

I. INTRODUCTION

Technological applications of optoelectronic devices based on (0001), i.e., *c*-oriented GaN are complicated by the piezoelectric effect along the [0001] direction. This phenomenon gives rise to a band bending, known as the quantum confined Stark effect.[1] Nonpolar or semipolar GaN thin films overcome this problem. However, this type of material possesses a large number of defects, especially stacking faults (SFs) so that a reliable method for the determination of the defect densities is of high importance. Several works have been published on the application of x-ray diffraction for the determination of the density of defects in a-plane oriented GaN epitaxial layers [*a*-GaN, surface $(11\bar{2}0)$] (see the review in Ref. 2), most of them are based on the well-known Warren theory of diffuse scattering from stacking faults in hcp crystals.[3] This description was originally developed for polycrystals and the density of SFs is determined from the full widths at half maximum (FWHM) of several diffraction peaks.[4] In Ref. 5, the components of the microstrain tensor in an *a*-GaN have been determined from the analysis of the reciprocal-space distribution of the diffracted intensity (RSM). RSM of *a*-GaN layers and transmission electron microscopy (TEM) have been used in Ref. 6 for the determination of the SF density, the authors find a linear calibration curve connecting the density of the SFs in (0001) planes with the FWHM of the diffraction maximum.

The defect structure of *m*-oriented GaN layers [surface $(1\bar{1}00)$] is similar to *a*-GaN. The density of (0001)-oriented SFs in these layers was determined from x-ray diffraction data using a modified Williamson-Hall method;[7] this approach determines the mean size of coherent crystal blocks between adjacent fault planes from the FWHM of the diffraction peaks in the [0001] direction perpendicular to the fault planes.

The FWHM of diffraction maxima are affected not only by SFs but also by other defects, especially dislocations and mosaic blocks. In contrast to the previous works mentioned above, in this paper we investigate not only the widths of the diffraction peaks but also full shapes of the maxima in reciprocal space. This method makes it possible to distinguish the peak broadening due to SFs from the contribution of other defects. The full shape of the diffraction maximum makes it possible to determine not only the density but also the prevalent type of the SFs. However, as we show later, this task requires to measure the diffracted intensity very far from the diffraction maximum, which was not the task of the present study.

We develop a theoretical description of diffuse scattering from SFs and perform a series of numerical simulations. The description is based on a Monte Carlo approach, in which we calculate the reciprocal-space distribution of the x-ray intensity diffusely scattered from a random set of stacking faults; a similar approach has been used in a row of papers for the investigation of hcp to fcc martensitic transition.[8,9] The applicability of our method is tested on a set of *a*-GaN epitaxial layers with various SF densities.

The paper is organized as follows. First, we give the sample description and the experimental setup and x-ray measurements (Sec. I). Then, we develop our theoretical approach for the calculation of the intensity distribution (Sec. II). In Sec. III, we compare results obtained from the experimental and the theoretical part of this investigation and determine the densities of SFs in our samples.

II. EXPERIMENTAL

We investigated a series of four samples, denoted S1 to S4, grown heteroepitaxially on *r*-oriented sapphire substrates by metalorganic vapor-phase epitaxy (MOVPE) in an AIXTRON 200/RF-S horizontal flow reactor. Trimethyl gallium (TMGa), trimethyl aluminum, and ammonia (NH_3) have been used as Ga, Al, and N precursors as described in more detail elsewhere.[10] We have chosen a series of samples with different growth conditions and different densities of defects. Before starting the growth, the substrate was heated up to 1200 °C for a desorption of surface impurities. Then, the growth of all samples was initiated with an about 20-nm-thick high-temperature AlN nucleation layer. For sample S1, this was followed by a

GaN film deposited at the same temperature of 1120 °C and a NH_3 to TMGa molar flow ratio (V/III ratio) of about 1100 to a total thickness of approximately 2.2 μm. In order to optimize the GaN layer quality, we have applied a two-step procedure to sample S3 where we increased the V/III ratio in the first step to a value of about 2200 for the growth of the first 1 μm, owing to achieve best bulk crystal quality. Then, we reduced this parameter to about 540 for the growth of the top layer (2.3 μm) in order to minimize the surface roughness. For sample S2, we grew a first 1-μm-thick GaN layer applying an increased V/III ratio of about 2200, where a defect-reducing *in situ* deposited SiN layer was integrated after 300 nm, similar as described in Ref. 11. Then, a second SiN layer was deposited before about 2.3 μm GaN were grown with reduced V/III ratio of about 540. For sample S4, a template according to S3 was additionally overgrown by hydride vapor phase epitaxy to a total thickness of approximately 9 μm (see Ref. 10 for more details).

The x-ray diffraction (XRD) experiments were performed using a custom-built rotating-anode setup with a small focus (Cu anode, 2 kW output). A double-bent parabolic multilayer mirror and a Ge(220) channel cut monochromator were used to produce a well collimated beam of CuKα_1 radiation with the divergences of about 12 arcsec and less than 0.1 deg in the scattering plane and across it, respectively. The primary beam was shaped by slits down to the cross section of 1×1 mm^2, the source-sample distance was about 1.6 m. For data collection, a linear multichannel detector with the pixel size of about 50 μm at a distance of 0.8 m to the sample was used.

As we show later, the SFs in the (0001) basal planes (so called basal SFs) give rise to a narrow streak in reciprocal space along [0001]. For the determination of the SF density, it is necessary to measure the intensity distribution along this streak, therefore the [0001] direction must be parallel to the scattering plane (common plane of the wave vectors $\boldsymbol{K}_{i,f}$ of the primary and scattered waves, respectively). In a coplanar scattering geometry, the scattering plane is perpendicular to the sample surface, i.e., to $(11\bar{2}0)$ plane in case of *a*-GaN. All coplanar diffractions in this scattering plane are of the type $11\bar{2}L$, however, as we show in the theory section, all basal SFs do not produce any diffuse scattering in these diffractions. Therefore we used an inclined geometry (see Fig. 1) in which the scattering plane makes an angle of 30 deg with the surface normal $\boldsymbol{n} = \frac{1}{3}[11\bar{2}0]$ and symmetric diffractions $H0\bar{H}0$. The inclined geometry was the reason for the collimation of the primary beam in two orthogonal directions described above.

In the inclined geometry, we measured RSMs in diffractions with $H = 1,2,3$. The resolution in reciprocal plane is determined by the divergence of the primary x-ray beam both in the scattering plane and perpendicular to it, by the pixel size of the detector and its distance from the sample. For the experimental conditions listed above, we achieved a resolution better than 0.05 nm^{-1} for all measured diffractions in both directions in the scattering plane.

III. STRUCTURE MODEL OF STACKING FAULTS

It is well established nowadays that wurtzite *a*-GaN epitaxial layers contain a large amount of planar defects (stacking faults SFs) in addition to dislocations of various types.[2,6,12] Three types of intrinsic (I1, I2, and I3) as well as one type

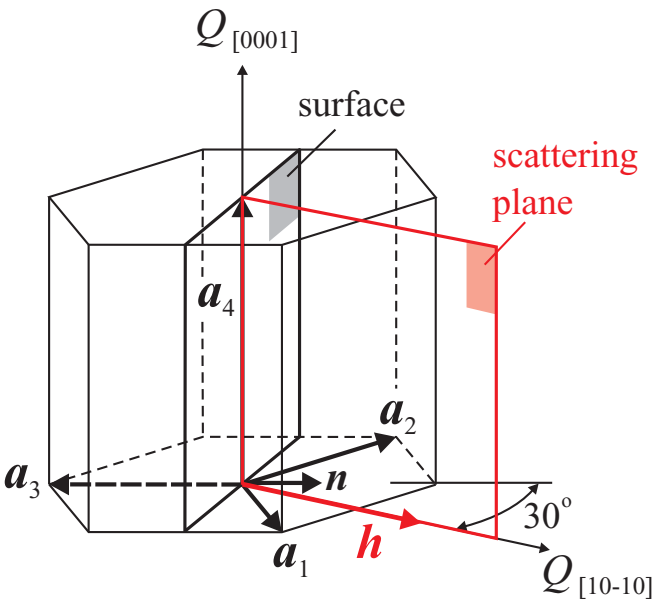

FIG. 1. (Color online) The sketch of the elementary unit cell of wurtzite GaN with the orientation of the *a* plane (grey) and scattering plane (red). The scattering plane makes an angle of 30 deg with the surface normal $\boldsymbol{n}$.

of extrinsic (E) basal SFs occur in (0001) planes and also prismatic SFs in planes $\frac{1}{2}\{10\bar{1}1\}$ are reported in the literature. In this section, we restrict ourselves to the most common basal SFs I1–I3 and E.[13] The stacking of the (0001) basal planes in these defect types is displayed in Fig. 2.

Developing the formula for the intensity scattered from a random sequence of SFs, we assume that the GaN layer diffracts kinematically, i.e., effects of dynamical x-ray diffraction (including absorption and refraction) are fully neglected. This simplification is fully justified if (i) the GaN layer is much thinner than the x-ray extinction length in GaN (about

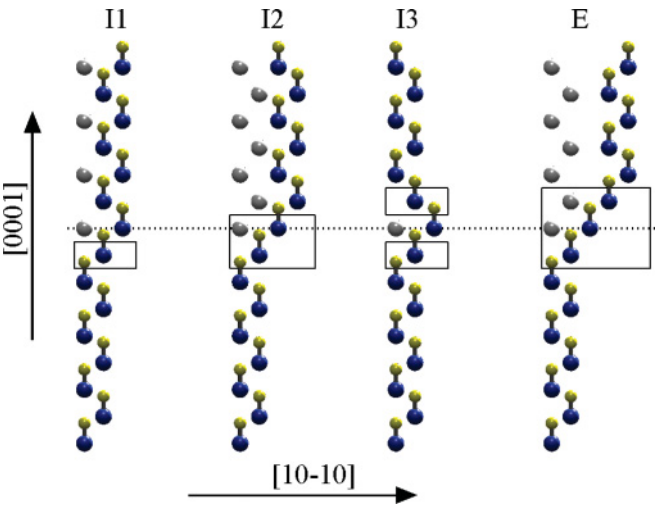

FIG. 2. (Color online) Sketch of the positions of Ga (blue) and N atoms (yellow) in various types of basal stacking faults. The fault plane is denoted by the dotted line. The black rectangles denote the segments with fcc-like stacking. Grey spheres denote the Ga positions in an ideal lattice.

3 μm in diffraction $20\bar{2}0$ and CuKα_1 radiation) or the angular deviation from the diffraction maximum is larger than the width of the intrinsic Darwin curve, and (ii) the incidence and/or exit angles of the x-ray beams are much larger than the critical angle of total external reflection (0.33 deg for CuKα_1). Further, we assume the validity of the far-field limit, i.e., the size of the coherently irradiated sample area (below 1 μm in a usual experimental arrangement) is much smaller than the diameter of the first Fresnel zone. The positions of individual SFs are assumed random and the irradiated sample volume contains a large number of defects so that the measured x-ray signal can be assumed averaged over a statistical ensemble of all configurations of the SFs.

First, let us consider a perfect layer without any structural defects. Using the kinematical approximation and the far-field limit introduced above, the amplitude of the wave diffracted from the layer is a function of the scattering vector $\boldsymbol{Q} = \boldsymbol{K}_f - \boldsymbol{K}_i$ (the difference of the wave vectors of the diffracted and primary beams):

$$E(\boldsymbol{Q}) = A[f_{\mathrm{Ga}}(Q) + f_{\mathrm{N}}(Q)\mathrm{e}^{-\mathrm{i}\boldsymbol{Q}\cdot\boldsymbol{d}}]\sum_{\boldsymbol{n}}\mathrm{e}^{-\mathrm{i}\boldsymbol{Q}\cdot\boldsymbol{R}_{\boldsymbol{n}}}. \quad (1)$$

Here, we denoted $f_{\mathrm{Ga,N}}$ the form-factors of atoms Ga and N, $\boldsymbol{d} = 3\boldsymbol{a}_4/8$ is the position vector of the N atom with respect to Ga in a GaN molecule, and $\boldsymbol{n} \equiv (n_1,n_2,n_3)$ are the indexes of a GaN molecule with the position vector $\boldsymbol{R}_{\boldsymbol{n}}$. The hexagonal basis vectors are $\boldsymbol{a}_{1,2,4}$, the vectors $\boldsymbol{a}_{1,2}$ and $\boldsymbol{a}_3 = -\boldsymbol{a}_1 - \boldsymbol{a}_2$ lie in the basal plane (0001), and $\boldsymbol{a}_4$ is orthogonal to it (see Fig. 2). A is a constant containing the amplitude of the primary beam, the classical electron radius, and the polarization factor, among others.

Since two GaN molecules constitute one GaN elementary unit cell, the molecule position vectors can be written as

$$\boldsymbol{R}_{\boldsymbol{n}} = n_1\boldsymbol{a}_1 + n_2\boldsymbol{a}_2 + n_3\boldsymbol{a}_4/2 + \sigma_{n_3}\boldsymbol{p}, \quad (2)$$

where $\boldsymbol{p} = \frac{2}{3}\boldsymbol{a}_1 + \frac{1}{3}\boldsymbol{a}_2$ is the lateral shift of the second Ga-N bilayer in the elementary unit cell with respect to the first one; we denote these bilayers by Bb and Aa, respectively. The ideal hcp stacking of bilayers is therefore denoted as ...AaBbAaBb..., the fcc stacking of the bilayers would be ...AaBbCcAaBbCc.... Further, $n_3 \equiv \sigma_{n_3}\mathrm{mod}(2)$, i.e., σ_{n_3} equals 0 (1) for even (odd) values of n_3, i.e., $\sigma_{n_3} = \sigma_{n_3-2}$ holds. For a general stacking sequence of bilayers Aa, Bb, and Cc, σ_{n_3} values create a general sequence of 0, 1, and 2. The case $\sigma_{n_3} = 3$ is equivalent to $\sigma_{n_3} = 0$, since $3\boldsymbol{p}$ is an integer linear combination of basis vectors $\boldsymbol{a}_{1,2}$. Therefore all the σ values are considered *modulo* 3.

Now, let us assume that the layer contains a single SF of type I1 in position $n_3 = n_{\mathrm{def}}$. The actual stacking sequence is then (we omit the symbols abc for the N atoms) ...ABABCBCB...for n_{def} even or ...ABACACA...for n_{def} odd. The corresponding sequences of the σ_{n_3} values are ...01012121...or ...0102020.... In both cases,

$$\sigma_{n_{\mathrm{def}}} \equiv \left(2\sigma_{n_{\mathrm{def}}-1} - \sigma_{n_{\mathrm{def}}-2}\right)\mathrm{mod}(3). \quad (3)$$

Using the same procedure, we find that the SF I2 in position n_{def} is described by the formulas

$$\begin{aligned}\sigma_{n_{\mathrm{def}}} &\equiv \left(2\sigma_{n_{\mathrm{def}}-1} - \sigma_{n_{\mathrm{def}}-2}\right)\mathrm{mod}(3),\\ \sigma_{n_{\mathrm{def}}+1} &\equiv \left(2\sigma_{n_{\mathrm{def}}} - \sigma_{n_{\mathrm{def}}-1}\right)\mathrm{mod}(3).\end{aligned} \quad (4)$$

The formulas for the type I3 are

$$\begin{aligned}\sigma_{n_{\mathrm{def}}} &\equiv \left(2\sigma_{n_{\mathrm{def}}-1} - \sigma_{n_{\mathrm{def}}-2}\right)\mathrm{mod}(3),\\ \sigma_{n_{\mathrm{def}}+1} &\equiv \sigma_{n_{\mathrm{def}}-1}\mathrm{mod}(3),\\ \sigma_{n_{\mathrm{def}}+2} &\equiv \left(2\sigma_{n_{\mathrm{def}}+1} - \sigma_{n_{\mathrm{def}}}\right)\mathrm{mod}(3).\end{aligned} \quad (5)$$

The SF of the extrinsic type (E) is described by

$$\begin{aligned}\sigma_{n_{\mathrm{def}}} &\equiv \left(2\sigma_{n_{\mathrm{def}}-1} - \sigma_{n_{\mathrm{def}}-2}\right)\mathrm{mod}(3),\\ \sigma_{n_{\mathrm{def}}+1} &\equiv \left(2\sigma_{n_{\mathrm{def}}} - \sigma_{n_{\mathrm{def}}-1}\right)\mathrm{mod}(3),\\ \sigma_{n_{\mathrm{def}}+2} &\equiv \left(2\sigma_{n_{\mathrm{def}}+1} - \sigma_{n_{\mathrm{def}}}\right)\mathrm{mod}(3).\end{aligned} \quad (6)$$

The stacking sequences of various SF types are represented graphically in Fig. 2, from which Eqs. (3)–(6) follow as well. From the figure, it follows that the SFs are represented by short fcc-like segments; in the case I1, for instance, the fcc segment contains one (0001) bilayer, in I2, the fcc segment consists of two bilayers.

A given microscopic distribution of stacking faults is described by a certain sequence of the values of σ_{n_3}, from which the diffracted amplitude can be calculated:

$$E(\boldsymbol{Q}) = \Phi(\boldsymbol{Q})\sum_{n_3=0}^{N}\xi^{n_3}\kappa^{\sigma_{n_3}}, \quad (7)$$

where

$$\Phi(\boldsymbol{Q}) = A[f_{\mathrm{Ga}}(Q) + f_{\mathrm{N}}(Q)\mathrm{e}^{-\mathrm{i}\boldsymbol{Q}\cdot\boldsymbol{d}}]\sum_{n_1,n_2}\mathrm{e}^{-\mathrm{i}\boldsymbol{Q}\cdot(n_1\boldsymbol{a}_1+n_2\boldsymbol{a}_2)},$$
$$\xi = \mathrm{e}^{-\mathrm{i}\boldsymbol{Q}\cdot\boldsymbol{a}_4/2}, \quad \kappa = \mathrm{e}^{-\mathrm{i}\boldsymbol{Q}\cdot\boldsymbol{p}},$$

and N is the number of coherently irradiated (0001) basal planes. The range of the double sum $\sum_{n_1,n_2}$ corresponds to the lateral size S of the stacking faults and we assume that this size is comparable to the layer thickness. Then, the function $\Phi(\boldsymbol{Q})$ gives rise to a narrow streak in reciprocal space along [0001], i.e., perpendicular to the SF planes (0001). The width of the cross section of this streak can be estimated to $2\pi/S$ and it is usually comparable to the resolution limit of the experimental setup. Therefore, in the following, we deal only with the reciprocal-space distribution of diffracted intensity $I(Q_{[0001]})$ along the SF streak.

The reciprocal-space distribution of the intensity stemming from one coherently irradiated volume is given by a convolution of the function $|E(Q_{[0001]})|^2$ with the resolution function $\Gamma(Q)$ of the experimental device:

$$\begin{aligned}I(Q) &= \int dQ'|E(Q-Q')|^2\Gamma(Q'),\\ \Gamma(Q) &= \int_{-\infty}^{\infty}dx\,\Gamma(x)\mathrm{e}^{-\mathrm{i}Qx}.\end{aligned} \quad (8)$$

The resolution function is the Fourier transformation of the mutual coherence function of the primary radiation $\Gamma(x)$ in two points in the distance x along the [0001] direction. However, the numerical calculation of the integral in Eq. (8) is time consuming and we used the following approximate approach

instead. We define the function $\Psi(x) = \sqrt{\Gamma(x)}$ and instead of calculating the convolution in Eq. (8) we use the formulas:

$$E(\boldsymbol{Q}) = \Phi(\boldsymbol{Q}) \sum_{n_3=0}^{N} \xi^{n_3} \kappa^{\sigma_{n_3}} \Psi(n_3|\boldsymbol{a}_4|/2),$$
$$I(Q_{[0001]}) = |E(Q_{[0001]})|^2. \tag{9}$$

The function $\Psi(x)$ describes a broadening of the diffraction curve not only due to a limited coherence of the primary beam but also due to other effects such as limited angular resolution of the detector and diffuse scattering from other defect types, like dislocations. As we show later, the form of this function can be determined from the diffraction curve measured around the reciprocal lattice point $\boldsymbol{h}$, where the SFs do not produce any diffuse scattering.

In a standard x-ray diffraction experiment, the irradiated sample volume is much larger than the coherence volume of the primary beam, so that the measured diffracted intensity is an incoherent superposition of intensities originating in various coherently irradiated volumes. From this fact, the calculation strategy follows: (i) in a coherently irradiated volume consisting of N (0001), Ga-N bilayers we define the positions and types of the SFs using a suitable random generator (see below). (ii) From the positions and types of the SFs defined in the previous step we construct the sequence of σ's using Eqs. (3)–(6). (iii) We calculate the amplitude of the diffracted wave using Eq. (9) and the diffracted intensity $I_j = |E_j|^2$. (iv) We repeat the items (1)–(3) M times and obtain the intensities I_j, $j = 1, \ldots, M$. Each intensity distribution I_j corresponds to the intensity scattered for a single coherently irradiated volume, M is the number of these volumes in the irradiated sample volume. (v) We calculate the average intensity profile

$$I(Q_{[0001]}) = \frac{1}{M} \sum_{j-1}^{M} I_j(Q_{[0001]}) \tag{10}$$

and the root-mean-square (rms) deviation σ_I of the average intensity[14]

$$\sigma_I^2 = \frac{1}{M}\left[\frac{1}{M}\sum_{j-1}^{M} I_j^2 - \left(\frac{1}{M}\sum_{j-1}^{M} I_j\right)^2\right]. \tag{11}$$

Increasing the number M of coherently irradiated volumes, the rms deviation σ_I decreases. The simulation procedure is rather time consuming so that we were not able to use the actual number M given by the experimental conditions. Instead, we chose M so that the maximum of $\sigma_I(Q_{[0001]})$ did not exceed 5%; the resulting computation time was few minutes for a scan of about 10^3 values of $Q_{[0001]}$.

For the definition of random positions of the SFs, we assume that the sequence of the SFs of *the same type* creates a homogeneous Markov chain.[15] The distances D_n between the $(n-1)$th and nth SFs are expressed in integer multiples of $|\boldsymbol{a}_4|/2 \equiv c/2$ ($c = 5.186$ Å is the vertical lattice parameter of wurtzite GaN), and they are assumed random and uncorrelated. In the simulations, we used the geometric distribution of the distances with the mean value $\langle D_0 \rangle = D_0$ and rms deviation $\sigma_D = \sqrt{\langle (D-D_0)^2 \rangle} = \sqrt{D_0(D_0+1)}$; for this distribution, we obtain the best correspondence of the measured and simulated intensity profiles. We tried also the Poisson distribution, however, in this case we obtain broad but well visible satellite maxima on the SF streak with the mean distance of about $\Delta Q_{[0001]} = 2\pi/D_0$, which are not observed in the experimental data.

The geometric distribution is a discrete analog of the exponential distribution. The probability of finding the (dimensionless) distance D is $w(D) = p(1-p)^D$, where the parameter p is the probability of finding the SF in a given position, connected with the mean value D_0 of D by $D_0 = (1-p)/p$. The geometric distribution is the only discrete "memoryless" distribution in which the probability of finding the SF in the given position does not depend on actual positions of other SFs.[16] Further, we assumed that the mutual positions of the SFs of different types are statistically uncorrelated so that the total diffracted intensity is a sum of contributions of the Markov chains of various defect types.

We have performed an extensive series of simulations for various defect types and densities and for various diffractions $\boldsymbol{h} = H0\bar{H}0$, $H = 1,2,3$ in symmetrical inclined scattering geometry (Fig. 1). In diffraction $H0\bar{H}0$ the factor κ occurring in Eqs. (7) and (9) for diffracted intensity is $\kappa = \mathrm{e}^{-4\pi \mathrm{i} H/3}$, which equals $(-1 \pm \mathrm{i}\sqrt{3})/2$ for $H = 1,2$, respectively, and $\kappa = 1$ for $H = 3$. Therefore, in diffraction $\boldsymbol{h} = 30\bar{3}0$, the SFs of all types assumed here do not produce diffuse scattering and the broadening of the diffraction maximum along the SF streak is caused either by experimental resolution or by diffuse scattering from other defect types. Thus the $30\bar{3}0$ diffraction can be used for the determination of the function $\Psi(x)$ defined above. It is worthy to note that in asymmetric coplanar diffractions $11\bar{2}L$ $\kappa = 1$ holds as well, so that these diffractions are not suitable for the measurement. The condition of the "visibility" of a basal SF, $\kappa \neq 1$, is equivalent to the condition $\boldsymbol{h} \cdot \boldsymbol{R} \neq$ integer, where $\boldsymbol{R}$ is the stacking fault displacement vector.[2,17]

In the sum $\sum_{n_3}$ for the diffraction amplitude, the segments with $\kappa^{\sigma_{n_3}} = (-1 + \mathrm{i}\sqrt{3})/2$ and $(-1 - \mathrm{i}\sqrt{3})/2$ appear in average with the same occurrence for $H = 1$ and 2, therefore the intensity distributions in diffractions $10\bar{1}0$ and $20\bar{2}0$ differ only due to different values of atomic form-factors $f_{\mathrm{Ga,N}}(Q)$. Figure 3 presents the intensity distributions along the SF streak calculated for different SF types depicted in Fig. 2. In the simulations, we used the same mean distance between the fault planes $D_0 = 50$ (expressed in mutliples of $c/2$) and we put $\Psi(x) = 1$, i.e., we assumed a perfectly plane incident wave and no diffuse scattering from other defect types. Figure 3 displays the intensity distributions calculated along the $[10\bar{1}L]$ rod crossing also the diffraction maxima $[10\bar{1}\bar{2}]$, $[10\bar{1}\bar{1}]$, $[10\bar{1}1]$, and $[10\bar{1}2]$.

From Fig. 3(b), it follows that the shapes of the diffuse scattering maxima from the defects of types I1 and I2 are almost identical in the vicinity of the reciprocal lattice points and these defect types can be distinguished only from the intensity distributions around the anti-Bragg points $L = n + \frac{1}{2}$. Close to a reciprocal lattice point, the intensities from both defect types are proportional to $Q_{[0001]}^{-2}$; this behavior follows from the geometric distribution of the SF distances. From Fig. 2, it is obvious that the sequence ...ABAB...is inverted to ...CBCB...in the case of I1, and the sequence ...ABAB...is

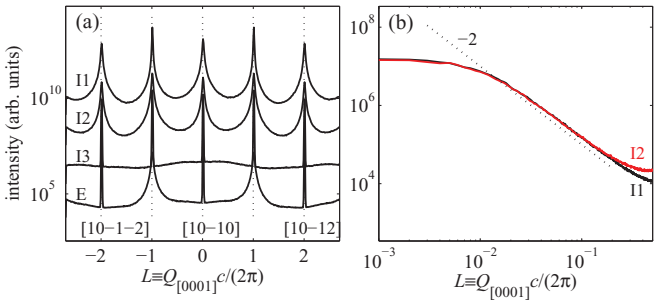

FIG. 3. (Color online) (a) Intensity distributions along the SF streak calculated in diffraction $10\bar{1}0$ for various types of the SFs and the same mean distance $D_0 = 50$ between the SFs; the curves are shifted vertically for clarity and an ideally coherent primary beam was assumed ($W \to \infty$). Diffraction maxima along the $[10\bar{1}L]$ rod are indicated by vertical dotted lines. (b) Detail of the diffraction maximum of defects I1 and I2 in loglog scale, the dotted line represents the slope −2.

shifted to ...CACA...for I2. This inversion or shift of the lattice gives rise to a shift in phase of the scattered wave and the diffuse scattering along the SF streak is produced by the interference of the phase-shifted waves originating from various hcp segments divided by the SFs. On the other hand, in the case of the I3 defect, the hcp segments on both sides of the defect are in phase. Therefore diffuse scattering from I3 is caused only by pairs of very narrow fcc segments connected to each fault plane. This is the reason, why the intensity distribution along the $[10\bar{1}L]$ rod does not exhibit any maximum around the reciprocal lattice point [see Fig. 3(a)]. In the case of defects E, the diffuse scattering along the $[10\bar{1}L]$ rod is concentrated around every second reciprocal lattice point, i.e., $[10\bar{1}\bar{3}]$,$[10\bar{1}\bar{1}]$,$[10\bar{1}1]$,$[10\bar{1}3]$, etc.

The width of the intensity maximum along the SF streak is inversely proportional to the mean distance D_0 between the SFs I1 or I2. This is demonstrated in Fig. 4, where we present the intensity curves calculated in diffraction $10\bar{1}0$ for various D_0. Nevertheless, the FWHM of the diffraction curve cannot be used for the determination of D_0, since the shape of the diffraction maximum and its FWHM in particular are affected by the function $\Psi(x)$; this is shown in Fig. 5, where the diffraction curves calculated for various widths of $\Psi(x)$ are plotted. In the simulations, we assumed that the function can be described by the well-known PearsonVII distribution function:[18]

$$\Psi(x) = \left[1 + 4(2^{1/\alpha} - 1)\left(\frac{2x}{W}\right)^2\right]^{-\alpha},$$

where W is the FWHM of the function and α is the shape parameter. For $\alpha \to \infty$, this function approaches the Gauss function, in the case of $\alpha = 1$, $\Psi(x)$ corresponds to the Lorentz function. The case $W \to \infty$ represents an ideally coherent and plane primary wave and no diffuse scattering from other defects (dislocations in particular). Decreasing W, the resulting diffraction curve changes its form and its FWHM increases. In order to discriminate the influence of this effect from the true intensity profile, it is necessary to measure the intensity curves in various diffractions $H0\bar{H}0$. As we showed above, the diffraction curve in $30\bar{3}0$ is not

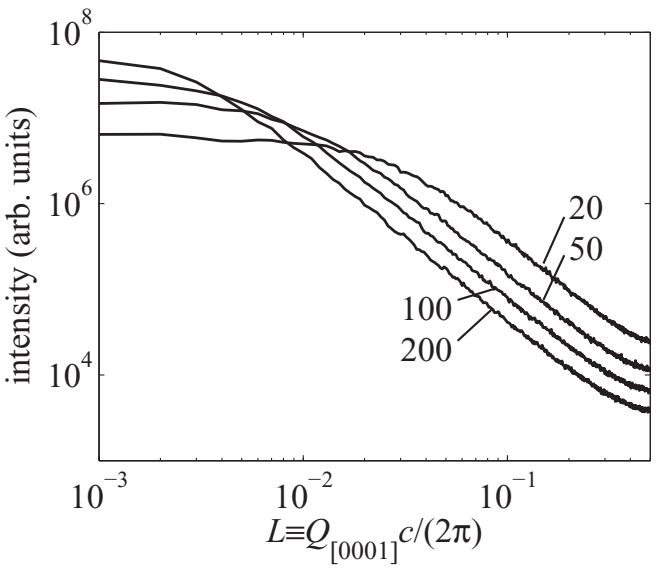

FIG. 4. Intensity distributions along the SF streak calculated in diffraction $10\bar{1}0$ for various mean distances D_0 expressed in integer multiples of $c/2$. Ideally coherent primary beam was assumed ($W \to \infty$).

affected by the SFs at all so that from its form the parameters W and α of function $\Psi(x)$ can be determined; these values can be used for the analysis of diffraction curves in other diffractions. However, both the effect of transversal coherence and diffuse scattering from dislocations scale with the length of the diffraction vector $\boldsymbol{h}$. Therefore the FWHM W_H of the function $\Psi(x)$ in diffraction $H0\bar{H}0$ is

$$W_H = 3/H \times W_3, \tag{12}$$

where W_3 is the FWHM determined from diffraction $30\bar{3}0$. The shape parameter α does not depend on the diffraction order H.

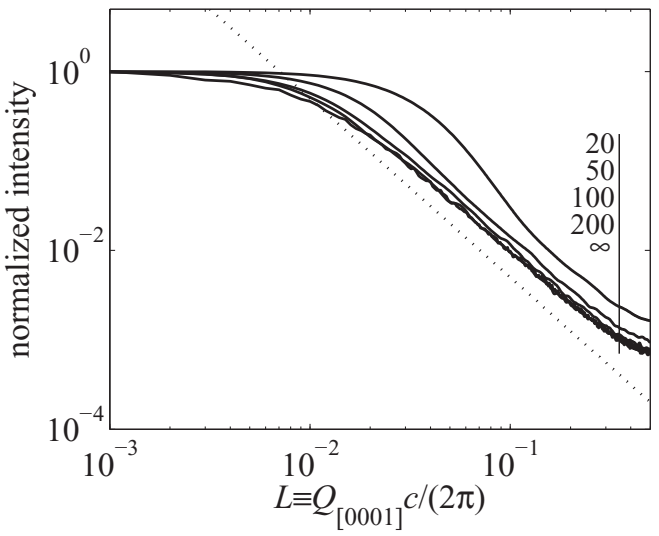

FIG. 5. Intensity distributions along the SF streak calculated in diffraction $10\bar{1}0$ for various widths W of the function $\Psi(x)$ expressed in integer multiples of $c/2$ and constant $D_0 = 50$. The dotted line represents the slope −2.

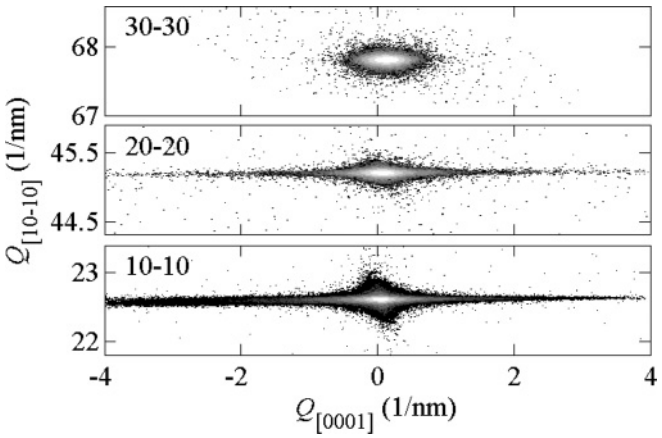

FIG. 6. Examples of the reciprocal space maps of x-ray diffuse scattering measured in the symmetric noncoplanar diffractions $10\bar{1}0$, $20\bar{2}0$, and $30\bar{3}0$ (from the top to the bottom, respectively) of the sample S3. The data are plotted in a logarithmic scale, the step of the isointensity levels is $10^{0.5}$. The SF streaks in diffractions $10\bar{1}0$ and $20\bar{2}0$ are clearly visible.

IV. RESULTS AND DISCUSSION

Figure 6 displays the RSMs of sample S3 measured in diffractions $10\bar{1}0$, $20\bar{2}0$, and $30\bar{3}0$; the RSMs of other samples are similar. The [0001]-oriented streak is visible in $10\bar{1}0$ and $20\bar{2}0$ diffractions, while the diffraction maximum in $30\bar{3}0$ is rather round. According to the theory above, this feature indicates the presence of basal SFs. To determine the density of SFS, from the RSMs we extracted intensity scans along the [0001]; these scans for sample S3 are plotted in Fig. 7. We tested several procedures for extraction, the best way was to integrate the measured RSM in a narrow stripe of the width $\Delta Q_{[10\bar{1}0]} = 0.1$ nm^{-1} around the maximum; this integration effectively suppresses the experimental noise. The inset in Fig. 7 shows the intensity maxima in detail; from the inset, it follows that the FWHM of the $20\bar{2}0$ and $30\bar{3}0$

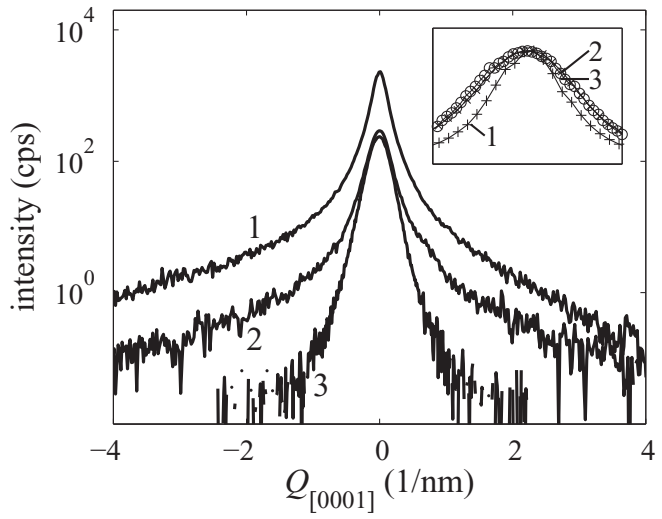

FIG. 7. Linear scans in [0001] direction (i.e., along the SF streak) extracted from the RSMs in Fig. 6. The inset shows the details of the scan around the maximum, normalized to maximum intensity. The numbers denote the orders H of the diffractions $H0\bar{H}0$.

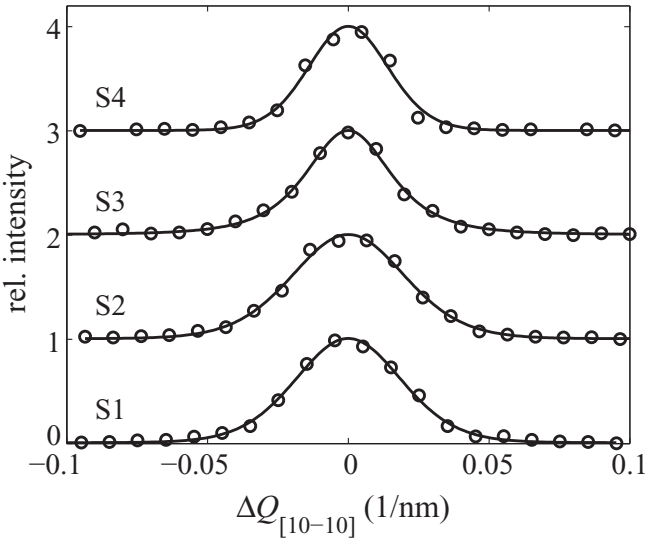

FIG. 8. Linear scans in $[10\bar{1}0]$ direction (i.e, across the SF streak) extracted from the RSMs of all samples in diffraction $10\bar{1}0$ for $Q_{[0001]} = 2$ nm^{-1} (points) as well as their fits by Gaussian functions (lines). The scans are shifted vertically for clarity.

are almost identical, i.e., the FWHM is affected mainly by the function Ψ and not by the diffuse scattering from the SFs.

Figure 7 demonstrates that the extracted intensity scans are slightly asymmetric, this asymmetry is stronger for smaller H. This effect is of purely geometrical nature; for $Q_{[0001]} < 0$, the irradiated sample volume (and consequently the number of irradiated SFs) is larger than for $Q_{[0001]} > 0$. We included this effect in the intensity simulations by multiplying the intensity by the factor $1/\sin(\alpha_i)$, where α_i is the variable incidence angle of the primary x-ray beam.

We have also extracted scans across the SF streaks at $Q_{[0001]} = 2$ nm^{-1}; Fig. 8 displays these scans for all samples in diffraction $10\bar{1}0$ and their fits by Gaussian functions. From the FWHM of these scans, we determined the effective sizes S_{eff} of the SFs, their values are in Table I. These values represent the lower limits of the true sizes S, since the linear scans are considerably broadened by the experimental resolution.

We fitted the measured [0001] scans to the theory described in the previous section. First, we determined the FWHM W of function Ψ defined in Eq. (9) from the scans in diffraction $30\bar{3}0$, in which the SFs do not cause diffuse scattering; the values of W are in Table I. Then, using these values of W and taking into account the scaling property in Eq. (12), we fitted the intensity scans measured in diffractions $10\bar{1}0$ and $20\bar{2}0$. The measured and fitted scans are plotted in Fig. 9; the measured and calculated intensity scans agree very well. From the fits, we determined the dimensionless mean distances D_0 of the SFs and the SF density

$$\varrho = \frac{2}{cD_0}, \tag{13}$$

the density values are in Table I as well.

From the theory, it follows that the FWHM of the [0001] scans in diffractions $10\bar{1}0$ and $20\bar{2}0$ are equal and therefore the SF densities ϱ should not depend on the diffraction order H. However, the density values in Table I sometimes slightly

TABLE I. Densities of the SFs determined from diffractions $10\bar{1}0$ and $20\bar{2}0$ for samples S1 to S4, the mean densities $\langle\varrho\rangle$ from both diffractions, the effective widths S_{eff} of the SFs, and the widths W of the functions $\Psi(x)$ determined from diffraction $30\bar{3}0$. The density values are determined with an accuracy of approximately $\pm 10\%$, the errors of S_{eff} and W are approximately 10 and 0.1 nm, respectively.

Sample	$\varrho_{10\bar{1}0}$ (10^5 cm^{-1})	$\varrho_{20\bar{2}0}$ (10^5 cm^{-1})	$\langle\varrho\rangle$ (10^5 cm^{-1})	S_{eff} (nm)	W (nm)
S1	4.1	4.1	4.1	140	8.6
S2	4.0	2.6	3.3	130	13.0
S3	3.2	3.8	3.5	180	11.7
S4	2.6	2.7	2.65	190	15.8

differ; the reason of this difference is not completely clear yet. It could be caused by the difference in the information depths, from which the diffuse scattering is collected. The incidence and exit angles in $20\bar{2}0$ are larger than in $10\bar{1}0$, therefore the SF density determined from $20\bar{2}0$ is averaged over a layer thickness of about 14 μm, while $10\bar{1}0$ probes only an approximately 5-μm thick layer. The largest difference in the defect densities was observed in sample S2, where $\varrho_{20\bar{2}0} < \varrho_{10\bar{1}0}$. This sample however contains a defect-reducing SiN layer buried in the GaN volume, so that the defect density in the surface layer is expected smaller than below the SiN layer. Therefore the effect of the information depth cannot explain this difference. Another possible explanation of the difference in the $\varrho_{10\bar{1}0,20\bar{2}0}$ values could be an inhomogeneous distribution of the defects in the layer volume (bunching of the defects), which has not been included in the theory. The irradiated sample surface in diffraction $10\bar{1}0$ is larger than in $20\bar{2}0$, so that the latter diffraction could be more sensitive to a possible bunching effect. Other structural imperfections like surface roughness or macroscopic sample bending cannot explain this difference.

Sample S4 exhibits the smallest SF density. This finding corresponds nicely to our expectations that any defects are reduced by overgrowing our samples with a thick high-quality GaN layer. The FWHM W of the function $\Psi(x)$ include both the experimental resolution and diffuse x-ray scattering from other defects. The density of these defects can be hardly determined, qualitatively it increases with decreasing W.

In contrast to other works published so far, our method determines the SF density from the whole intensity profiles of the SF streak. If the SF streak is visible in the measured reciprocal-space intensity distribution, the influence of the stacking faults can be distinguished from other defects.

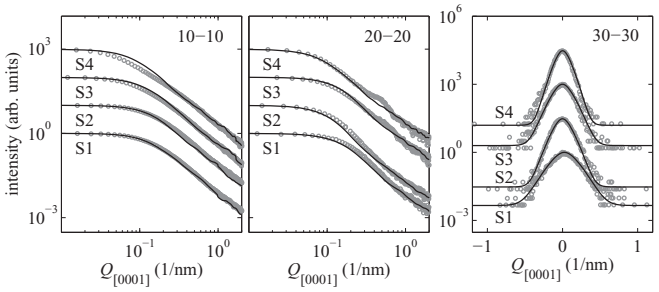

FIG. 9. Experimental (circles) and theoretical (solid lines) intensity scans along the [0001] direction in the $10\bar{1}0$ diffractions $10\bar{1}0$ (left), $20\bar{2}0$ (middle), and $30\bar{3}0$ (the right panel). The numbers of the samples are indicated, the curves are shifted vertically for clarity.

Roughly speaking, the SF density is proportional to the FWHM of the SF streak, however the whole intensity profile has to be taken into account. The minimum SF density (i.e., the maximum mean distance between adjacent fault planes) can be estimated from the minimum measurable broadening of the diffraction maximum in [0001] direction, which in our case is determined mainly by the angular resolution of the detector. For our geometry, the minimum detectable SF density is about 10^4 cm^{-1}.

We have restricted our experiments to a small vicinity of the reciprocal lattice points $H0\bar{H}0$, this restriction did not allow us to distinguish between the types I1 and I2 of the SFs; the SF types I3 and E can be excluded. The resolution of the defect type from the [0001] scans could be possible if we measure the scans around the anti-Bragg points $L = n + 1/2$, this will be the subject of our next paper. Nevertheless, the SF densities in Table I most likely apply to the I1 defects, since about 90% of all defects are of type I1[2] because of their lower formation energy than the other defect types.[12,19]

V. SUMMARY

We have developed a theoretical description of diffuse scattering from a random set of basal stacking faults in *a*-plane GaN epitaxial layers. We have simulated the distributions of the diffusely scattered x-ray intensity in direction perpendicular to the fault planes, i.e., along the [0001] lines in reciprocal space crossing the reciprocal lattice points $H0\bar{H}0$ ($H = 1,2,3$). From the comparison of the simulations with experimental data on a series of GaN samples, we determined the density of basal stacking faults. The method makes it possible to distinguish between the diffuse scattering from stacking faults and the effects of other structural defects.

ACKNOWLEDGMENTS

We thank S. Lazarev, B. Miljevic, and S. Bauer (KIT Karlsruhe) for useful scientific discussions. Preliminary x-ray diffraction measurements have been carried out at Institute of Physics AS CR Prague, Czech Republic by O. Pacherová, J. Kub, and Z. Šourek. The influence of the information depth on the value of the defect density was suggested by one of the referees. The work is a part of the research program MSM 0021620834 financed by the Ministry of Education of the Czech Republic; the work was supported by the Charles University (projects Nos. 22310 and 263307) as well. The financial support of parts of this work by the Deutsche Forschungsgemeinschaft within the Research Group PolarCoN is gratefully acknowledged.

[1]F. Bernardini, V. Fiorentini, and D. Vanderbilt, Rhys. Rev. B **56**, R10024 (1997).
[2]M. A. Moram and M. E. Vickers, Rep. Prog. Phys. **72**, 036512 (2009).
[3]B. E. Warren, *X-Ray Diffraction* (Dover Publications, New York, 1990).
[4]Q. S. Paduano, D. W. Weyburne, and A. J. Drehman, Phys. Status Solidi A **207**, 2446 (2010).
[5]R. N. Kyutt, M. P. Shcheglov, V. V. Ratnikov, and A. E. Kalmykov, Phys. Status Solidi A **206**, 1757 (2009).
[6]M. A. Moram, C. F. Johnston, M. J. Kappers, and C. J. Hupmhreys, Physica B **404**, 2189 (2009).
[7]M. B. McLaurin, A. Hirai, E. Young, F. Wu, and J. S. Speck, Jpn. J. Appl. Phys. **47**, 5429 (2008).
[8]R. Berliner and S. A. Werner, Phys. Rev. B **34**, 3586 (1986).
[9]V. K. Kabra and D. Pandey, Acta Crystallogr. Sect. A **51**, 329 (1995).
[10]S. Schwaiger, F. Lipski, T. Wunderer, and F. Scholz, Phys. Status Solidi C **7**, 2069 (2010).
[11]J. Hertkorn, F. Lipski, P. Brückner, T. Wunderer, S. B. Thapa, F. Scholz, A. Chuvilin, U. Kaiser, M. Beer, and J. Zweck, J. Cryst. Growth **310**, 4867 (2008).
[12]D. N. Zakharov, Z. Liliental-Weber, B. Wagner, Z. J. Reitmeier, E. A. Preble, and R. F. Davis, Phys Rev. B **71**, 235334 (2005).
[13]M. A. Moram, C. F. Johnston, J. L. Hollander, M. J. Kappers, and C. J. Hupmhreys, J. Appl. Phys. **105**, 113501 (2009).
[14]V. M. Kaganer, O. Brandt, H. Riechert, and K. K. Sabelfeld, Phys. Rev. B **80**, 033306 (2009).
[15]D. T. Gillespie, *Markov Processes: an Introduction for Physical Scientists* (Academic Press, San Diego, 1992).
[16]A. N. Shiryaev, *Probability* (Springer, New York, 1996).
[17]D. C. Williams and C. B. Carter, *Transmission Electron Microscopy* (Springer, Berlin, 1996).
[18]M. M. Hall, V. G. Veeraraghavan, H. Rubin, and P. G. Winchell, J. Appl. Cryst. **10**, 66 (1977).
[19]R. Liu, A. Bell, F. A. Ponce, C. Q. Chen, J. W. Yang, and M. A. Khan, Appl. Phys. Lett. **86**, 021908 (2005).